

Atomistic Insights into the Oxidation of Flat and Stepped Platinum Surfaces Using Large-Scale Machine Learning Potential-Based Grand-Canonical Monte Carlo

Jiayan Xu, Wenbo Xie, Yulan Han, and P. Hu*



Cite This: ACS Catal. 2022, 12, 14812–14824



Read Online

ACCESS |

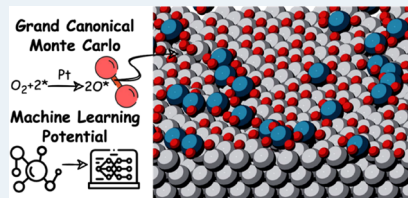
Metrics & More

Article Recommendations

Supporting Information

ABSTRACT: Understanding catalyst surface structure changes under reactive conditions has become an important topic with the increasing interest in operando measurement and modeling. In this work, we develop a workflow to build machine learning potentials (MLPs) for simulating complicated chemical systems with large spatial and time scales, in which the committee model strategy equips the MLP with uncertainty estimation, enabling the active learning protocol. The methods are applied to constructing PtO_x MLP based on explored configurations from bulk oxides to amorphous oxidized surfaces, which cover most ordered high-oxygen-coverage platinum surfaces within an accessible energy range. This MLP is used to perform large-scale grand canonical Monte Carlo simulations to track detailed structure changes during oxidations of flat and stepped Pt surfaces, which is normally inaccessible to costly ab initio calculations. These structural evolution trajectories reveal the stages of surface oxidation without laborious manual construction of surface models. We identify the building blocks of oxide formation and elucidate the surface oxide formation mechanism on Pt surfaces. The insightful interpretations would deeply help us understand the oxide formation on other metal surfaces. We demonstrate that these large-scale simulations would be a powerful tool to investigate realistic structures and the formation mechanisms of complicated systems.

KEYWORDS: machine learning potential, density functional theory, grand canonical Monte Carlo, surface oxidation, platinum surfaces



1. INTRODUCTION

Platinum has been widely utilized in various catalytic systems; for example, it is the catalyst for CO oxidation and the electrode material in electrocatalysis.^{1,2} Most platinum-based catalytic reactions are performed under oxygen-rich conditions in which the platinum surface can be partially oxidized.^{3–8} Moreover, the formed surface oxides appear to have higher catalytic reactivity compared to metal surfaces.^{9–12} It is impossible to understand the corresponding catalytic performances without revealing the detailed structures of the surface oxides. Currently, the investigation of surface oxidation is hindered by technical limitations both in experimental and theoretical methods. Most experimental studies examined the surface oxidation under ultrahigh vacuum conditions, which should be very different from real conditions.¹³ On the other hand, theoretical studies proposed several high-symmetric structures at different O coverages, which were only obtained from small unit cells due to the considerable computational cost of density functional theory (DFT) calculations for large systems.^{14–18} According to the phase diagram produced by ab initio thermodynamics,^{19,20} the stability of different O-adsorbed Pt surfaces could be acquired.²¹ However, there is no guarantee that these manually constructed surface models can represent the structures formed under real reactive conditions. It is expected that the formation of large-scale high-symmetric structures may be difficult even under well-designed experiments, let alone operando conditions.²² The

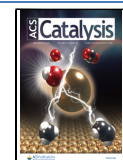
lack of atomic details for the oxidation process hampers the understanding of the formation of active surface oxides. In fact, none of the formation mechanisms of any metal surface oxide is clear.

To obtain plausible insights into surface oxidation from computational work, it is necessary to carry out large-scale simulations that explore a variety of configurations of surface oxides. The on-lattice Monte Carlo simulation is one of the methods with acceptable computational cost, which has been widely utilized in the kinetic Monte Carlo for transition metals.^{23–25} This method simplifies the catalyst surface as a rigid grid and ignores the interaction between adsorbates and the surface lattice, which makes it difficult to simulate amorphous surface systems.²⁶ On the contrary, off-lattice grand canonical Monte Carlo (GCMC) has no limits on the surface lattice and is more suitable for the investigation of the oxidation process.^{27,28} Since GCMC involves a large number of total energy calculations, reliable simulations using DFT have only been applied to small unit cells.²⁹ When more realistic

Received: August 11, 2022

Revised: October 3, 2022

Published: November 22, 2022



modeling is necessary, i.e., large unit cells are considered, simulations are possible if more computationally efficient methods are used. For example, ReaxFF potential has been developed for PtO_x systems to study the surface oxidation.^{30–35} The GCMC/ReaxFF simulations of Pt(111) oxidation at near-ambient pressure (1 mbar) produced consistent results with experiments for oxygen coverages as a function of time.³⁴ However, this simulation was performed on a small unit cell and the accuracy of ReaxFF was not validated on disordered surface oxides. More importantly, the formation mechanism of PtO_x surface oxides observed in experiments, such as the raised Pt atom and PtO_2 stripe, remains ambiguous.

The oxidation process involves both ordered and disordered systems with different chemical compositions, which include bulk oxides, oxide surfaces, and surface oxides. Therefore, realistic modeling requires comprehensive exploration of the potential energy surface at the DFT-level accuracy. To address this complexity among all these distinct systems, machine learning potentials (MLPs) are promising methods due to their near-DFT accuracy and small computation cost.³⁶ Unlike conventional force field methods that are governed by specific formulae, MLPs learn the relationship between atomic energy and its local chemical representation. Recent efforts are devoted to developing nonlocal equivalent representation with explicit Coulomb and vdW interactions,^{37,38} namely, REANN,³⁹ Nequip,⁴⁰ and SpookyNet.⁴¹ Currently, the dataset construction is another bottleneck of the MLP development. It is noteworthy that the Open Catalyst Project has been established to accelerate the MLP construction by providing a transparent platform to share high quality datasets and benchmark different models.⁴² It has released over 260 million DFT calculations of molecular relaxations, which aids model training and catalyst design. However, a generally applicable workflow does not exist to construct a dataset for arbitrary chemical systems, particularly for metal oxidation where different unit cell sizes and numbers of atoms should be taken into consideration. It is highly desirable to propose a workflow to automate the dataset construction. Another issue of concern in the application of MLPs is uncertainty quantification.^{43–55} The uncertainty estimation not only helps explore unlearned configurations in active learning but also ensures the reliability of calculation results in large systems where DFT results are not readily accessible.

In this work, we trained a neural network potential applicable for PtO_x systems, especially for structures generated in the oxidation of flat and stepped Pt surfaces. An efficient iterative active learning procedure was proposed to automate MLP training for chemical systems of interest. Large-scale GCMC simulations were performed to observe the oxidation of a flat $p(20 \times 20)$ Pt(111) surface and stepped $p(2 \times 12)$ Pt(17 15 15) surface at room temperature (300 K) and near-ambient pressure (1 mbar). After analyzing GCMC trajectories, we found that there are basically three stages for PtO_2 stripe formation on flat surfaces, which is the reason for the surface buckling, and discovered two vital surface structures responsible for the PtO_2 growth, namely, square-planar PtO_4 and minimal stripe Pt_2O_6 . Moreover, we elucidated the formation mechanism of octahedral PtO_6 found on the edge during the oxidation of stepped surfaces, which is related to the complete oxidation from the Pt surface to $\alpha\text{-PtO}_2$. All these formation mechanisms were further verified by DFT calculations.

2. COMPUTATIONAL METHODS

2.1. Electronic Structure Calculation. The electronic structure calculations for obtaining reference energies and forces were performed with Vienna ab initio simulation package.^{56,57} The exchange–correlation interaction was described by vdW-DF since van der Waals interactions play an important role in layered $\alpha\text{-PtO}_2$ and high-coverage surface oxides.^{58–60} The projector augmented wave pseudopotential with a cutoff energy of 400 eV was selected for core electrons. The k-points sampled in the Brillouin zone were Gamma-centered with a spacing of 0.05 Å⁻¹ in each direction of the reciprocal lattice.⁶¹

2.2. Techniques for Machine Learning Potential. The MLP assumes that the total energy of any geometrical configuration is the summation of atomic energies as $E = \sum_i E_i$. In this scheme, the construction of atomic energy E_i includes two steps. The first step is to transform each atom's Cartesian coordinates into a symmetry-preserved representation for its local chemical environment \mathcal{A}_i , which describes the spatial and elemental distribution of its neighbors within a finite cutoff R_c . Then, a regression model is trained to learn the complicated relationship between E_i and \mathcal{A}_i . In this work, we adopted the embedded atom neural network potential (EANNNP) developed by Zhang et al., which uses an embedded atom descriptor as the atomic representation and a deep neural network as the regression model.^{62,63} This model was demonstrated to have relatively better accuracy and less computational cost compared to other MLP frameworks.⁶⁴ The detailed formulae and training settings of EANNNP can be found in Section S1 in the Supporting Information (SI).

Since EANNNP adopts a deep neural network as the regressor, the model performance is largely determined by the training dataset. To evaluate the model prediction, we adopted the committee model uncertainty estimation.^{44,50} In this strategy, an ensemble of models is concurrently trained with different initializations of learnable parameters or different portions of the dataset, and the prediction uncertainty is estimated by the variance of these model outputs. For instance, the mean and variance of total energy prediction are given by

$$\bar{E} = \frac{1}{M} \sum_1^M E^i \quad (1)$$

$$\sigma^2(E) = \frac{1}{M-1} \sum_1^M |E^i - \bar{E}|^2 \quad (2)$$

where M is the number of models. This estimation can be used for other properties as well, such as forces and stresses. Due to the high nonlinearity of the neural network model and the randomness of the optimizer, the final converged models would be slightly different even with the same inputs. However, they would give consistent results on well-learned configurations while yielding large deviations on configurations far away from the training dataset. Therefore, the prediction uncertainty can help us determine whether the predictions are acceptable and whether new models have to be trained on an expanded dataset.

2.3. Grand Canonical Monte Carlo Simulation. GCMC simulation follows the principle of statistical mechanics and avoids the combinational explosion of possibilities in the equilibrium structures.²⁸ Besides, it provides a history-dependent evolution trajectory of the system. From the trajectory, not

only can equilibrated configurations be extracted, but also the formation process of the surface oxides can be observed. Since the simulation works in the grand canonical ensemble, the chemical potential μ , volume V , and temperature T of the system are fixed. In each step of a GCMC simulation, the system is allowed to interact with an external reservoir by two actions, namely, the move action and the exchange action. The probability of accepting an attempted “move” step is

$$P_{\text{move}} = \min(1, e^{-\Delta U/k_B T}) \quad (3)$$

where ΔU is the potential energy change after the action and k_B is the Boltzmann constant. The exchange step can be further divided into insertion and deletion. The probability of acceptance for insertion is

$$P_{\text{insert}} = \min\left(1, \frac{V}{(N+1)\Lambda^3} e^{-(\Delta U - \mu)/k_B T}\right) \quad (4)$$

where V is the system volume, N is the number of particles, and Λ is the thermal de Broglie wavelength as $\frac{\hbar}{\sqrt{2\pi m k_B T}}$. The probability of acceptance for deletion is

$$P_{\text{remove}} = \min\left(1, \frac{N\Lambda^3}{V} e^{-(\Delta U + \mu)/k_B T}\right) \quad (5)$$

In conventional GCMC, the simulation can be really time-consuming because a large number of attempts will generate high-energy configurations that have extremely low acceptance probability. To accelerate the simulation, we introduce a bias into the simulation, which performs a relaxation on the structure after each MC step. This bias can be balanced by revising the volume to effective volume in the probability calculation, which has been successfully applied in the previous studies.^{33,34,65,66}

In this work, we consider the oxidation of the Pt surface by O₂ gas. The fixed physical quantity in the system is μ_O , V , T , and N_{Pt} . The chemical potential of an oxygen atom can be approximately computed as

$$\mu_O(T, P) = \frac{1}{2} \mu_{O_2}(T, P) = \frac{1}{2} \left(G_{O_2}(T, P^\circ) + k_B T \ln\left(\frac{P}{P^\circ}\right) \right) \quad (6)$$

where P is the pressure of interest, and G_{O_2} is the Gibbs free energy of the oxygen molecule. We performed GCMC simulations with our in house code interfaced with LAMMPS using “eann pairwise”,⁶⁷ the implementation of which can be found in Section S2.

3. RESULTS

3.1. Dataset Construction. We integrated various exploration algorithms, including molecular dynamics (MD) and genetic algorithm (GA),^{68,69} model uncertainty estimation, and descriptor-based configuration selection^{70,71} to construct an efficient active learning pipeline. The pipeline via an open-sourced package named Generating Deep Potential with Python (GDPy).⁷² The brief introduction of it can be found in Section S3.

We started our research with the dataset construction of various platinum oxides (PtO_x). We first considered a variety of common bulk platinum oxides, such as PtO, α -PtO₂, β -PtO₂, and Pt₃O₄.⁷³ Previous experimental and theoretical studies demonstrated that α -PtO₂ and β -PtO₂ can be stable

phases under oxidative conditions.⁴ The DFT phase diagram showed that α -PtO₂ is the thermodynamically most stable phase at low temperatures, while Pt₃O₄ becomes more stable above 870 K.⁷⁴ Since the surface oxidation process is to be investigated, a few low-index oxide surfaces are considered as well, namely, PtO(100), PtO(101), α -PtO₂(0001), β -PtO₂(001), and Pt₃O₄(100).^{6,74,75} These surfaces have relatively low surface energies and can cover possible configurations during the conversion from surface oxides to bulk oxides. To further focus on the configurations that may occur on the flat and stepped platinum oxidation, we explored partial oxidations of the flat Pt(111) surfaces with various sizes and the stepped Pt surfaces that include Pt(211), Pt(533), and Pt(322), each of which further covers systems with a different amount of oxygen atoms. To this end, the entire PtO_x dataset consists of over two hundred thousand configurations. For training efficiency, we utilized structural descriptor-based selection to choose the most representative configurations of each system from the entire dataset, the procedure of which can be found in Section S3. The final training dataset has 58,784 structures, ten percent of which were used for the testset. The detailed list of the training dataset can be found in Section S4.

The overall performance of EANNP on the entire dataset reaches a root mean square error (RMSE) of 11 meV/atom and an RMSE in forces of 0.41 eV/Å for O and 0.21 eV/Å for Pt. We benchmarked EANNP against DFT on the lattice constants and surface energies (Section S5) and oxygen diffusion pathways on the flat Pt(111) surface (Section S6), which demonstrates that EANNP is very reliable. Furthermore, we tested our model committee on the dataset and observed that the prediction uncertainty is consistent with the true error, which can be found in Section S7.

3.2. Oxygen Coverage Convex Hull. The first step to understanding the oxidation process is to generate high-symmetry surfaces that have been reported extensively in previous studies. We utilized an automatic graph-theory-based evolutionary search⁷⁶ accelerated by EANNP to explore O-adsorbed Pt surfaces. The adsorption configurations were generated based on the adsorption-site graph and then optimized by EANNP. Our EANNP well reproduced the structures of adsorbed O atoms and surface oxides and their thermodynamic data, which demonstrates its accurate description of O–O and O–Pt interaction. Later, only the top one hundred stable structures predicted by EANNP were re-optimized by DFT calculations since the number of possible configurations of large unit cells was enormous. Therefore, the results presented in this section are all based on DFT calculations.

We define the surface formation energy as follows:

$$\gamma = \left(E_{\text{PtO}_y} - E_{\text{slab}} - y^* \frac{1}{2} E_{O_2} \right) / A^{hkl} \quad (7)$$

where A^{hkl} is the cross-sectional area of a given surface, in which hkl are the surface indices. The coverage of oxygen is defined as

$$\theta_O = N_O / N_{\text{pt}}^{\text{surf}} \quad (8)$$

where $N_{\text{pt}}^{\text{surf}}$ is the number of platinum atoms on the first layer.

We started the configuration exploration of adsorbed oxygens and surface oxides on the flat Pt(111) surfaces. We limited our search to five surfaces that can be calculated by

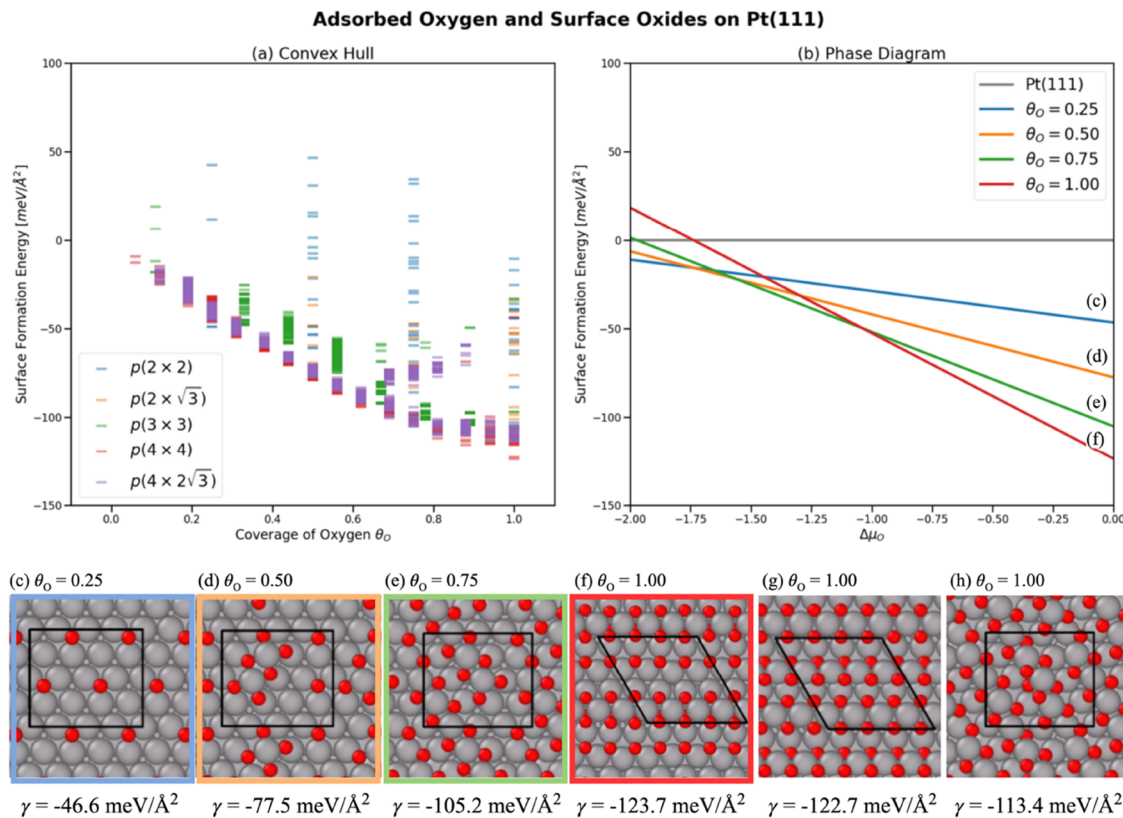


Figure 1. Convex hull of O on Pt(111) is shown in (a). The phase diagram made up of the most stable structures is shown in (b), the inset of which illustrates the coverages with colors corresponding to those in panels (c–f). Panels (g–h) exhibit two representative configurations at 1.0 ML coverage. At low coverages, O atoms all reside on FCC sites. When the coverage reaches a medium value (~0.5 ML), small PtO₂ stripes (containing two Pt atoms) are observed. With more O atoms adsorbed, O atoms start to migrate to the subsurface and many amorphous structures with similar formation energy can be generated.

DFT within an acceptable time, namely, $p(2 \times 2)$, $p(2 \times \sqrt{3})$, $p(3 \times 3)$, $p(4 \times 4)$, and $p(4 \times 2\sqrt{3})$. There are two stable adsorption sites on Pt(111), namely, the FCC site and the HCP site. The adsorption energies on these two sites are -1.38 and -0.97 eV on the $p(2 \times 2)$ unit cell corresponding to a coverage of 0.25 ML. Since the FCC sites are ca. 0.40 eV more stable than the HCP sites, a reasonable assumption is that oxygen should adsorb on the FCC sites at arbitrary surface coverages, which is adopted by a large number of microkinetic modeling and on-lattice kinetic Monte Carlo studies.^{24,25,77,78} However, this is not always the case when the coverage increases over 0.50 as we will demonstrate below.

In addition, there are also two tetrahedron subsurface sites that can be occupied by oxygen atoms, which have adsorption energies of 0.33 and 1.20 eV, respectively. The positive adsorption energies of these two sites indicate that the migration of oxygen atoms from the surface to the subsurface is highly thermodynamically unfavorable. The structures of these sites and their adsorption energies benchmarked with EANNNP are shown in Section S8.

For all the configurations related to adsorbed oxygen atoms and surface oxides on the flat Pt(111) surface, the generated convex hull and phase diagram with critical structures we discovered are illustrated in Figure 1. Figure 1a shows the convex hull constructed by 3199 configurations, which is made up of low-energy structures at each O coverage. In general, the surface formation energy of the most stable configuration gradually decreases with the increasing O coverage. This trend is not surprising since Pt surfaces would be oxidized to form a

more stable phase α -PtO₂ compared to simple O-adsorbed structures. It is obvious that there exist plenty of distinct configurations near the global minimum, which form a low-energy metastable ensemble. According to the Boltzmann distribution, these configurations have similar populations but may contain distinct reactivity due to their unique local chemical environments. Figure 1b illustrates the phase diagram obtained by the configurations at some selected coverages. The standard condition corresponds to $\Delta\mu_O$ of -0.25 eV, in which the configuration at 1.0 ML coverage would be the most favorable. Pt surfaces with lower coverages would dominate at elevated temperature or low pressure. However, the conditions of the realistic catalytic reactions often deviated from this condition; medium and high coverages of O atoms are more often the cases that should be focused on. Figure 1c–f shows the most stable structures at given coverages, while Figure 1g,h illustrates two structures at 1.0 ML coverage with low surface formation energies. Interestingly, it is found from the most stable configuration at each coverage that evolution from an ordered FCC adsorbed oxygen pattern to lifted surface PtO₂ stripes occurs.

At low O coverages smaller than 0.50 ML, adsorbed oxygen atoms are prone to occupy the FCC site and stay as far away from each other as possible, which forms a highly symmetric pattern. For instance, a configuration of 0.25 ML coverage (Figure 1c) shows that O resides at maximumly separated FCC sites to reduce the O–O lateral repulsion. When the coverage increases to 0.50 ML, the structures with all O atoms on the FCC sites can still be observed in the low-energy

Adsorbed Oxygen and Surface Oxides on Stepped Pt Surfaces

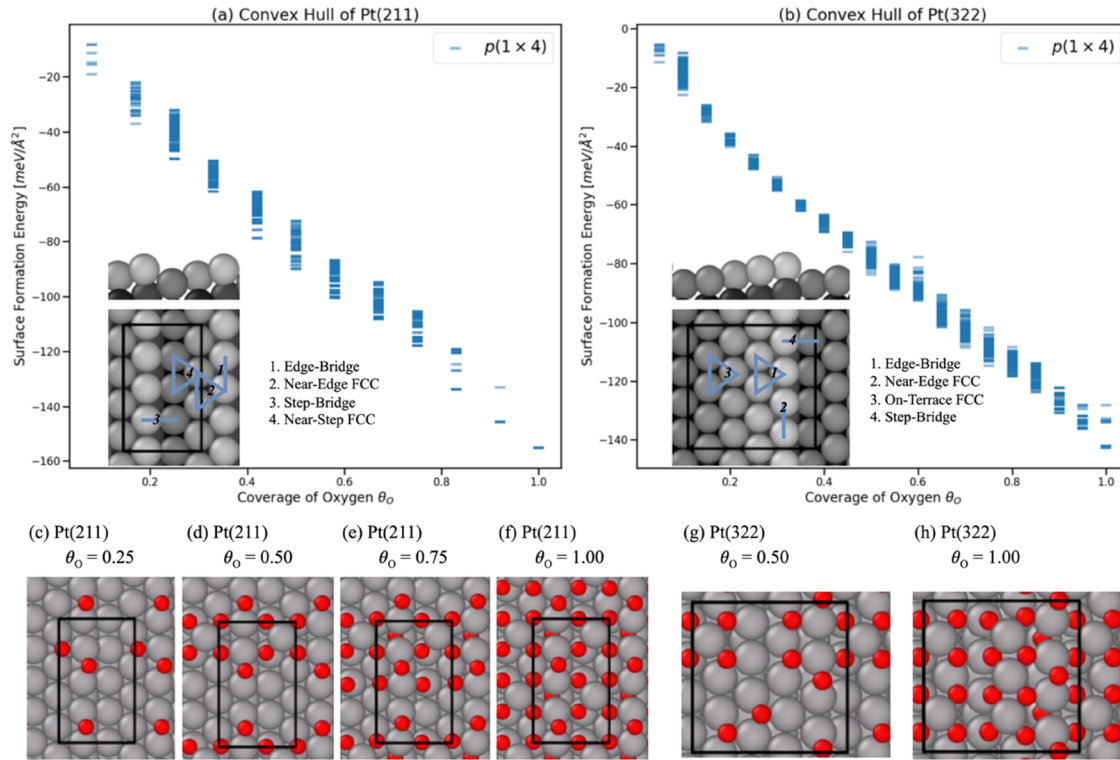


Figure 2. Results of structural exploration on stepped surfaces are illustrated. The convex hulls of Pt(211) and Pt(322) obtained by explored configurations at each coverage are shown in (a,b), respectively. The inset figures are structures of stepped surfaces, where blue triangles and lines denote the FCC and bridge adsorption sites, respectively. Panels (c–f) are the most stable configurations found in Pt(211) at each coverage, while (g,h) are two for Pt(322). O atoms prefer to adsorb on the edge-bridge and near-edge-FCC sites as in (c). Then, the square planar PtO_4 unit can be found on the terrace ((d,g)). Finally, the edge is oxidized to a distinguished Pt_2O_6 chain.

metastable ensemble. However, some Pt atoms would be lifted by adsorbed O atoms to form $\text{Pt}_n\text{O}_{2n+2}$ local structures that are a precursor of surface PtO_2 stripes. The structure in Figure 1d has a Pt_2O_6 motif that coexists with the FCC adsorbed O atoms, in which the protruded Pt atoms are 1.64 \AA above the flat surface.

With a further increase of coverage to 0.75 ML, the PtO_2 stripe continues to grow but with an incomplete PtO_3 end, as shown in Figure 1e. Similar structures with small PtO_2 stripes formed by adding extra O atoms to a $p(2 \times 1)$ -O layer were reported in a previous experimental study.⁷⁹ When the surface coverage increases to 1.0 ML, a low-energy ordered structure is found to have two Pt oxide rows as shown in Figure 1f; one is with five-coordinated Pt atoms, and the other one is simply with O atoms all on the FCC sites. This most stable configuration is in accordance with the previous computational results.³² The place-exchange Pt surface oxide is the second stable configuration as shown in Figure 1g, where one of two PtO_2 stripes rotates around the surface plane by 30 degrees.¹⁷ Moreover, we find that amorphous surface oxides can have very similar surface formation energy compared to some structures with ordered PtO_2 stripes. For example, O atoms start to migrate to subsurface sites created by raised Pt atoms (Figure 1h). The surface formation energy is only $2.2 \text{ meV}/\text{\AA}^2$ higher than the one reported in previous experimental studies⁸⁰ and also $10.3 \text{ meV}/\text{\AA}^2$ higher than the most stable one ($-113.4 \text{ meV}/\text{\AA}^2$ compared to $-123.7 \text{ meV}/\text{\AA}^2$). According to the results on the flat Pt surfaces, we can see

clearly that the most significant oxide unit is the square planar PtO_4 unit.

We also explored the configurations of adsorbed O atoms and surface oxides on the stepped Pt surfaces to elucidate the influence of steps on O adsorption. We took two vicinal-type surfaces with a (100) step for exploration, namely, Pt(211) and Pt(322). The stepped surfaces can be simply considered as the combination of a Pt(111) terrace and a step. Pt(211) can be viewed as $[3(111) \times (100)]$, while Pt(322) can be regarded to $[5(111) \times (100)]$. Considering adsorption sites on stepped surfaces, there are two kinds of twofold sites, such as the edge-bridge site and step-bridge site, and three kinds of threefold sites, namely, the on-terrace FCC site, near-edge FCC site, and near-step FCC site. On the $p(1 \times 4)$ Pt(211) surface, the favorable adsorption site on the terrace is the near-edge FCC site with an adsorption energy of -1.23 eV , while the favorable one on the edge is the twofold edge-bridge site that has an adsorption energy of -1.52 eV . This trend of preferable adsorption sites exists as well for the $p(1 \times 4)$ Pt(322) surface that has a decreased step–terrace ratio. These results are in accordance with previous computational studies.^{81–83} Therefore, O atoms would first reside on the edge-bridge sites and then the near-edge FCC sites. These basic adsorption sites on the stepped surfaces with their adsorption energies benchmarked with EANNNP are shown in Section S9.

The situation becomes complicated when the coverage increases since the surface Pt atoms can be elevated by O atoms. Figure 2 shows the convex hull formed by explored configurations and representative structures at some selected

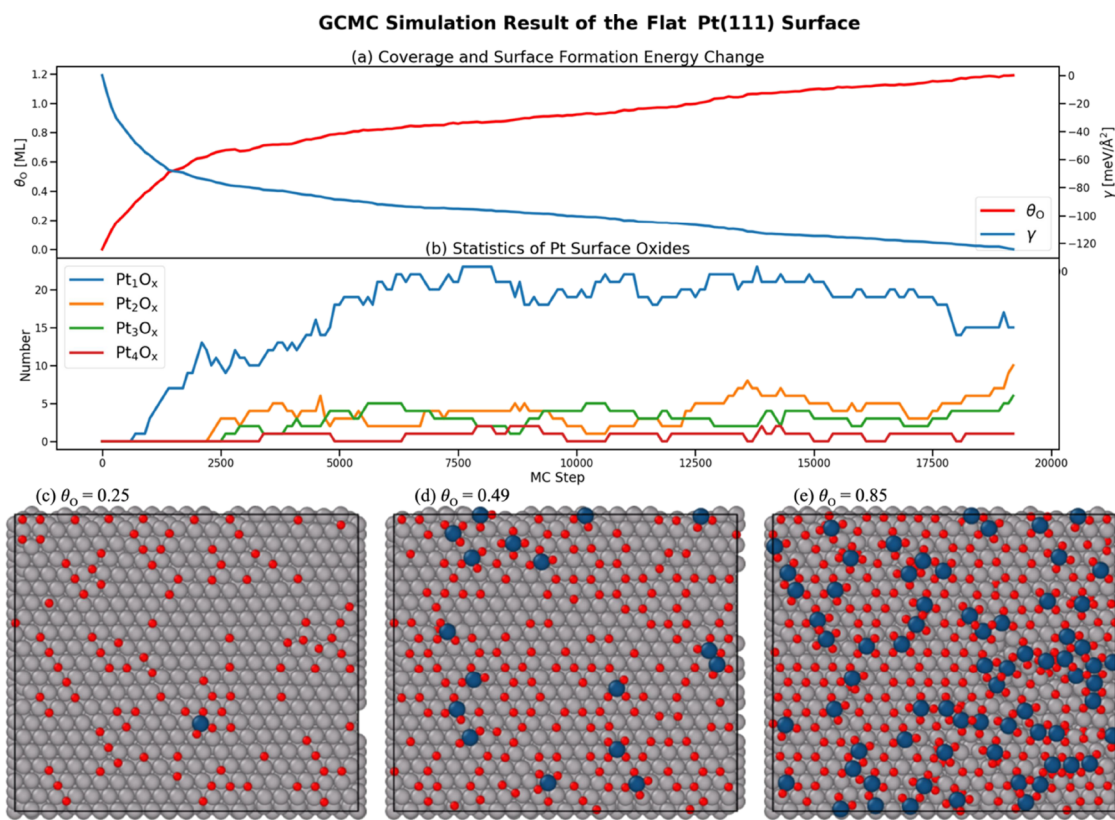


Figure 3. GCMC simulation results of the flat $p(20 \times 20)$ Pt(111) surface are illustrated. Panel (a) shows the changes in surface formation energies and O coverages during oxidation. Panel (b) shows the change in the number of local surface oxide units, such as the square planar PtO_4 unit and minimal PtO_2 stripe, which are two surface oxides responsible for the PtO_2 stripe formation. Panels (c–e) are representative structures at selected coverages. Blue balls are raised Pt atoms. The first raised Pt atom is found at 0.25 ML coverage, while the rest of Pt atoms adsorb on FCC sites. Plenty of square planar PtO_4 oxide units are observed at 0.49 ML coverage. The surface has already become disordered at 0.85 ML coverage, and longer PtO_2 stripes that contain three or more Pt atoms are found.

coverages. The convex hulls of Pt(211) and Pt(322) shown in Figure 2a,b, respectively, demonstrate that the surface formation energy decreases with the coverage increase, indicating that stepped surfaces are readily oxidized. Figure 2c–f shows the most stable structures at given coverages for Pt(211), while Figure 2g,h shows those for Pt(322).

At a low coverage (0.25 ML) on Pt(211) shown in Figure 2c, O atoms prefer to adsorb on the near-edge-FCC site and the edge-bridge site as we discussed on the adsorption sites of stepped surfaces. When the coverage increases to 0.50 ML, a Pt atom is lifted to form the planar square PtO_4 oxide unit (see Figure 2d) that is stabilized by the edge and the step simultaneously. When the coverage further increases to 0.75 ML (Figure 2e), we discover an interesting oxide motif with two square PtO_4 units that share a subsurface O atom. When reaching 1.0 ML coverage (see Figure 2f), the edge is largely oxidized to a PtO_3 chain, in which two neighbor Pt atoms are connected by a surface O atom or a subsurface one alternatively. Regarding Pt(322), we find that the square PtO_4 oxide unit on the terrace is more stable at the step bottom instead of near the edge, as shown in Figure 2g. When the coverage reaches 1.0 ML (Figure 2h), the configuration contains an edge PtO_3 chain. However, there are two kinds of Pt rows with planar square PtO_4 oxide units on the terrace. The first one is near the step and has raised planar square PtO_4 units that are separated by one Pt atom. The second one is a Pt_3O_8 stripe that contains three PtO_4 units. This difference demonstrates the influence of the step and edge on the

formation of the PtO_2 stripe. Perhaps more importantly, we find that the oxidized edge forms a PtO_3 chain that is different from the PtO_2 stripe on the flat surfaces and affects the vicinal stripe formation on the terrace.

3.3. GCMC Simulations. The configurations of adsorbed O atoms and surface oxides discussed above provide a basic overview of oxidized Pt surfaces. However, the connections between those static structures are not clear. In this work, we further performed large-scale GCMC simulations on the flat and stepped Pt surfaces to investigate the oxidation process at the atom level. These simulations not only can offer more distinct configurations and various local chemical environments but also provide fruitful insights into step-by-step oxidation mechanisms with their history-dependent trajectories. For the flat surface, we adopted a $p(20 \times 20)$ Pt(111) surface with eight Pt layers, which has 3200 Pt atoms in total. For the surface with steps, we utilized a $p(2 \times 12)$ Pt(17 15 15) surface that can be denoted as $[8(111) \times (100)]$, containing 1536 Pt atoms. All the simulations took at least 10,000 MC steps with the condition of 300 K and 1 mbar O_2 pressure to ensure that the final coverage exceeds 1.0 ML. Five independent simulations for each system were performed to make the results statistical observable. During all the simulations, the uncertainty of energy prediction has a small value of around 0.02 eV/atom and the relaxations are all converged to 0.05 eV/Å, which indicates that the optimized local minima are reasonable.

GCMC Simulation Result of the Stepped Pt Surface

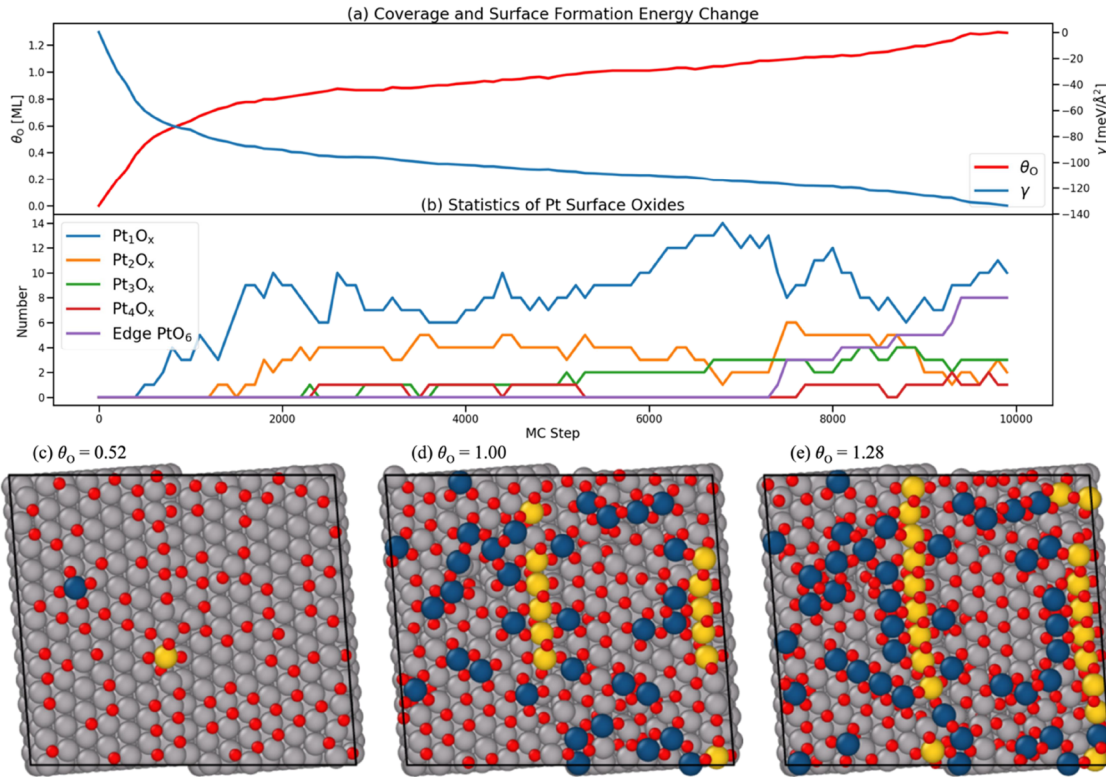


Figure 4. GCMC simulation results of the stepped $p(2 \times 12)$ Pt(17 15 15) surface are illustrated. Panel (a) shows the change of coverages and surface formation energies during the simulation. Panel (b) shows the change in the number of local surface oxide units, including raised Pt atom groups that contain one to four atoms and edge octahedral PtO_6 units. Panels (c–e) illustrate three representative structures at given coverages. Blue atoms are the raised Pt atoms, while yellow ones are the high-coordinated edge Pt atoms that have at least four O neighbors. During the early stage of the oxidation, Pt atoms on the terrace are first raised to form an on-surface square planar PtO_4 oxide unit, while Pt atoms on the edge are also oxidized to become a square planar PtO_4 unit but with one O atom in the subsurface. The further oxidation makes on-terrace PtO_2 stripes grow longer and the edge Pt atoms completely oxidized to sixfold-coordinated.

Figure 3 shows the changes in properties and representative structures at some selected coverages during one GCMC simulation. Figure 3a displays the change in surface formation energies and surface coverages during the oxidation. At the start of the simulation, the surface formation energy quickly drops with the increase of coverage. When the coverage is over 0.60 ML, the change of surface formation energies becomes much more moderate. Figure 3b illustrates the change in the number of local surface oxide structures defined by raised Pt atoms, where Pt atoms in the motif are connected by at least one O atom. The single raised Pt shows up at low coverage of around 0.25 ML, most of which are square planar PtO_4 . Pt_2O_x emerges at around 0.50 ML, and the structures that occur most often are rectangle Pt_2O_6 , which is consistent with the convex hull based on statically explored structures. Larger surface oxides appear later during the oxidation since they have to be generated from smaller raised Pt stripes. This observation implies that an interesting feature of the formation of the PtO_2 stripe is that Pt atoms are elevated one by one instead of being raised at the same time.

To further understand the oxidized structures, we selected three from low to high coverages for discussion. At the early stage of the oxidation corresponding to a coverage of 0.25 ML (Figure 3c), most O atoms will occupy their most favorable FCC sites, while the first Pt atom is found to be raised by its three O neighbors. We also notice that some oxygen atoms may adsorb on the HCP sites at first but move very quickly to

the more stable FCC sites. When the coverage increases to around 0.49 ML (see Figure 3d), there are a considerable number of raised Pt atoms. These buckled Pt oxides are mostly made up of T-shaped planar PtO_3 and square planar PtO_4 , in which the PtO_2 stripe can be considered as the minimum building block. Although there still exist some empty FCC sites, Pt atoms with three or more O neighbors are inevitably raised and further transformed into square planar PtO_4 units, which makes the surface locally buckle and opens a few oxygen migration pathways from the surface to the subsurface.³² This similar square-planar metal oxide unit was observed in our previous investigations of PdO_x .^{84–86} At 0.85 ML coverage, the surface becomes disordered and complicated Pt oxides are generated, as shown in Figure 3e. The square planar PtO_4 unit starts to grow into longer stripes, namely, Pt_2O_6 and Pt_3O_8 . We did not observe longer stripes before the top layer of the surface is completely oxidized (over 1.0 ML) since their formation may be hindered due to randomness.

Then, we moved on to the simulation of the stepped surface. Figure 4 shows the GCMC results of one representative trajectory. The changes of coverages and surface formation energies as shown in Figure 4a are very similar to ones from the Pt(111) surface. The surface formation energy decreases rapidly with the increase of O coverage. The energy decrease becomes much slower after the coverage reaches 0.60 ML. We also analyzed the number of change of local surface oxide structures defined in the same way as those on the flat surface

Surface PtO₂ Stripe Formation

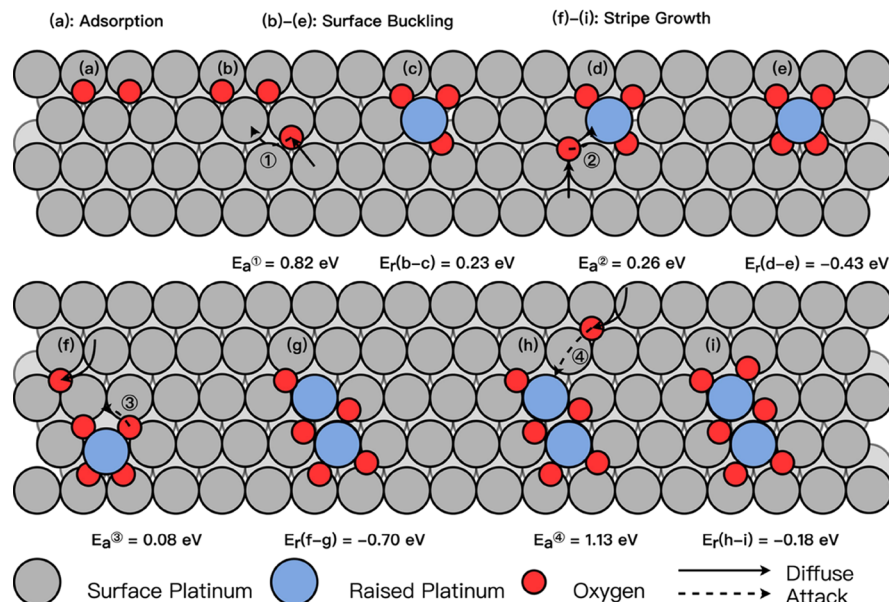


Figure 5. Formation mechanisms of two important surface oxides PtO₄ and Pt₂O₆ are illustrated. (a) Formation starts with adsorbed oxygen atoms. The square planar PtO₄ unit is the origin of the surface buckling and is formed by two oxygen atoms consecutively attacking the bridge sites, as shown from (b) to (e). Pt₂O₆ is generated based on a PtO₄ unit attacked by two extra oxygen atoms, as illustrated from (f) to (i), which is fundamental for the PtO₂ stripe growth.

and the sixfold-coordinated edge Pt atom, which is shown in Figure 4b. The first Pt atom raised on the terrace is observed at ca. 0.40 ML coverage. With more O atoms adsorbed, more Pt atoms on the terrace are elevated to group into local surface oxide units. When the coverage is over 1.00 ML, a few octahedral PtO₆ structures form, the Pt atom of which has the same local chemical environment as the one in α -PtO₂.

We show three structures at some selected coverages in the following. The structure at a medium coverage of 0.52 ML is basically ordered, as shown in Figure 4c. Most O atoms favor the edge-bridge and on-terrace-FCC sites. One Pt atom is raised on the terrace and forms a square planar PtO₄ unit that is the same as the one on the flat surface. Meanwhile, one edge Pt atom is found to form a square PtO₄ unit; however, one of its coordinated O atoms is in the subsurface. The structure at 1.00 ML coverage (Figure 4d) becomes disordered with more raised Pt atoms on the terrace and connected PtO₄ units on the edge. The Pt oxide on the edge is the PtO₃ chain that has already been identified and discussed in the structure exploration. Figure 4e shows a structure when the coverage increases to 1.28 ML. It is found that the surface PtO₂ stripes continue to grow and the longest one found in this simulation contains four Pt atoms. The edge PtO₃ chain is further oxidized to an α -PtO₂ stripe, in which every Pt atom is sixfold-coordinated.

3.4. Surface PtO_x Formation Mechanism. According to the results of GCMC simulations, we propose the formation mechanism of important surface oxide units, namely, raised PtO₄, minimal stripe Pt₂O₆, and edge PtO₆. These mechanisms were verified by DFT calculations on a flat $p(4 \times 4)$ Pt(111) surface and a stepped $p(1 \times 4)$ Pt(322) surface. The transition states were located by the climbing-image nudged elastic band method.⁸⁷

Figure 5 shows the formation mechanism from the FCC-adsorbed O atom to the Pt₂O₆ stripe via a key intermediate

that is the square planar PtO₄ oxide unit. The structure in Figure 5a where two O atoms adsorb on the neighbor FCC sites is very common at low coverages, which is discussed in Section 3.2. The PtO₄ formation starts with a local trimer structure as shown in Figure 5b where three oxygen atoms adsorb on the three neighbor FCC sites, which can be considered as the precursor of the surface buckling. Although the O atoms prefer to reside on the FCC sites at maximum separation due to the lateral repulsion, such local trimer structures can be frequently observed in GCMC simulations at low coverages (~ 0.25 ML). If the coverage further increases, there would even be a higher possibility of finding these trimers that are the origin of surface buckling. Once an oxygen atom attacks the bridge site, the central Pt atom will be lifted up by 1.5 Å to form PtO₃ as shown in Figure 5c, which has a reaction energy of 0.23 eV. This process has an energy barrier of 0.82 eV, which is very close to the barrier for oxygen diffusion through the bridge site (0.63 eV). With the buckled PtO₃ structure, an extra oxygen will attack the newly exposed buckled bridge site to form the square planar PtO₄ unit as shown in Figure 5d, in which the central Pt will be further lifted up by 0.2 Å. This process has an energy barrier of 0.26 eV and a reaction energy of -0.43 eV, indicating that the raised PtO₄ (Figure 5e) is thermodynamically favorable.

The Pt₂O₆ formation starts with the square planar PtO₄ oxide unit, which can be viewed as the fundamental process of the PtO₂ stripe growth. The second PtO₃ formation has a slightly different mechanism as shown in Figure 5f. The oxygen atom on the FCC site will attack the bridge site with a tiny rotation of the entire PtO₄ unit. Since the Pt atom under attack has already been coordinated by two O atoms, it ends up with a height increase of 1.2 Å as can be seen in Figure 5g. This process is almost barrierless (0.08 eV) and has a negative reaction energy of -0.70 eV, indicating that the stripe growth is favorable if the fifth oxygen atom is in the proper position.

Edge PtO₆ Formation

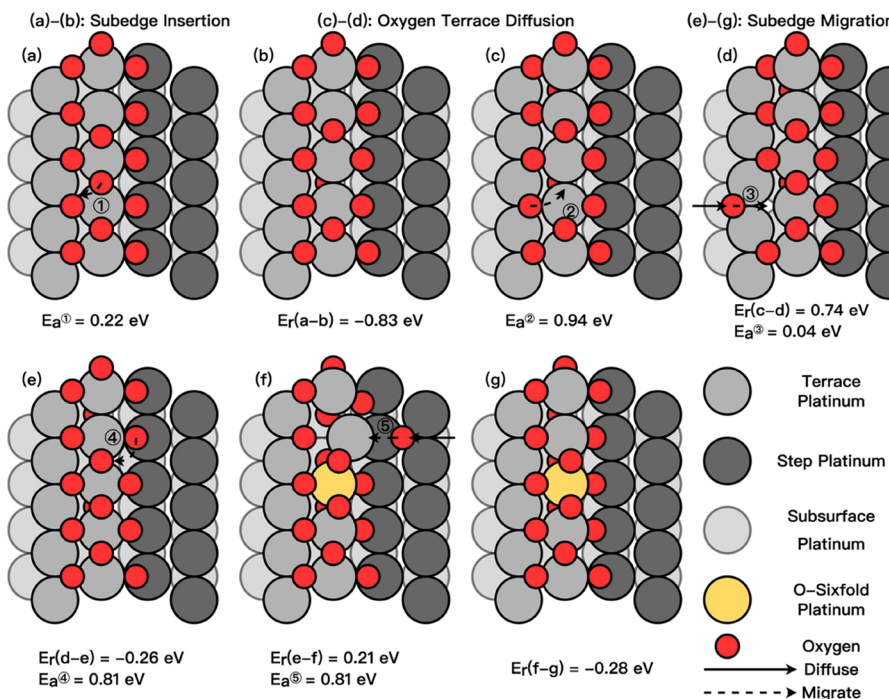


Figure 6. Formation mechanism of edge PtO₆ on the stepped Pt surface is illustrated. The formation starts with three vicinal O atoms on the edge-bridge sites. The sub-edge insertion from (a) to (b) generates a twin cross-plane square-planar PtO₄ unit, which is the first kind of formation of sub-edge oxygens. The on-terrace diffusion in (c,d) fills in the vacant edge-bridge sites. The reactions from (e) to (g) form the octahedral PtO₆ unit, during which one O atom migrates from the step-edge site to the sub-edge site as the second kind of formation of sub-edge oxygens.

The last step to form Pt₂O₆ (Figure 5h) is that an oxygen atom attacks the buckled bridge site through the atop site, which has an energy barrier of 1.13 eV similar to the surface diffusion. This process is thermodynamically favorable as well with a reaction energy of −0.18 eV. The final product is the Pt₂O₆ stripe with two Pt atoms raised, as shown in Figure 5i. Taken together, the stripe formation can be summarized into three stages: (a) O adsorption; (b–e) surface buckling with the appearance of the first PtO₄ unit; and (f–i) stripe growth with the neighbor Pt atom raised.

For the stepped Pt surface, we focused on the formation mechanism of the edge PtO₆ unit since the PtO₂ stripe identified on the terrace basically shares the same formation mechanism as the one on the flat surface. In the initial structure, the edge-FCC and step-bridge sites are fully occupied. The PtO₆ formation begins with three O atoms adsorbed on the edge-bridge sites as shown in Figure 6a. If one edge-bridge O migrates to the sub-edge site, the local structure would transform into a twin cross-plane square-planar PtO₄ unit as illustrated in Figure 6b. This process requires a moderate energy barrier of 0.22 eV, and the resulting structure is thermodynamically favorable with a reaction energy of −0.83 eV. Following this mechanism, the sub-edge sites would be occupied alternatively to form a PtO₃ chain as discussed in Section 3.2. Then, one O atom from a nearby FCC site migrates to the vacant edge-bridge site via the top of an edge Pt atom (Figure 6c), leading to a distorted O-fourfold Pt atom (Figure 6d). The migration barrier is 0.94 eV which is slightly smaller than the one from the FCC site to the HCP site via the top site (1.49 eV). Also, the released edge-FCC site will be filled in by an O atom on the neighbor FCC site. This migration is almost barrierless (0.04 eV) and has a negative

reaction energy of −0.26 eV since the introduced O atom stabilizes the distorted PtO₄ unit by forming an O-fivefold Pt atom as shown in Figure 6e. The formation of the octahedral PtO₆ unit begins with the migration of an O atom from the step-bridge site to the sub-edge site, which has an energy barrier of 0.81 eV and a reaction energy of 0.21 eV. The product shown in Figure 6f contains an octahedral PtO₆ unit and a distorted O-fourfold Pt atom that is further stabilized by the O atom migrated from a nearby step-FCC site. The reaction for the structure formation requires a barrier of 0.81 eV with a reaction energy of −0.28 eV (see Figure 6g). According to this formation mechanism, it is clear that there are three stages responsible for the appearance of sub-edge O atoms: (a,b) the direct insertion of an O atom from the edge-bridge site to the sub-edge one; (c,d) the O diffusion on the terrace that fills in vacant adsorption sites near the edge; and (e–g) the migration of an O atom on the step-FCC site to the sub-edge site during the completion of the octahedral PtO₆ unit. Moreover, this explains why the PtO₃ edge-chain should be an important intermediate for the complete oxidation of Pt surfaces.

4. DISCUSSION

Our constructed EANNP gives rise to consistent physical properties with DFT, such as lattice constants and surface energies, which should be suitable for studying the low-index ordered metal and oxide surfaces. It is also capable of determining optimal O adsorption configuration at various coverages, which is crucial to the study of the oxidation process. Our GCMC simulations demonstrate that a well-established EANNP equipped with uncertainty estimation is capable of simulating complicated structures using large unit

cells beyond standard DFT calculations. The training pipeline developed in this work can be readily transferred to other chemical systems, especially for systems with different chemical compositions. The uncertainty estimation is the core technique of the entire protocol since it helps us determine the unlearned configurations and ensure that the results from the productive simulations are accurate. This explores more portions of the configuration space and largely reduces the number of configurations that need expensive DFT calculations, which accelerates the entire workflow. Unlike traditional force field methods which usually give rise to inaccessible prediction errors, MLPs with uncertainty estimation are actively improvable according to the configuration space accessed by the production. The committee model adopted in our work was demonstrated to be effective both in the training and the production. However, there are still two issues that may affect the performance of MLPs. First, MLPs would inevitably inherit the shortcomings of the reference method, in most cases, DFT. For example, there is a considerable error in the DFT-calculated total energy of the O₂ molecule. The experimental bond energy is -5.161 eV (498 kJ/mol), while the vdW-DF result that we adopted is -6.214 eV (PBE -6.746 eV), which makes each O atom more stable by 0.53 eV. Though it may affect the phase diagram, i.e., the equilibrium configuration at given temperature and pressure, this energy error would not affect the intermediate structures found in GCMC simulations and their formation mechanisms. Second, the common framework of MLPs only treats short-range interatomic interaction by a local atomic representation. As an extension of EANN, REANN uses a recursive framework to include nonlocal effects to further improve the model accuracy.³⁹ In addition, the constructed dataset was also determined by the sampling algorithms. Since we focused more on the local minima in the study of surface oxidation, MD and GA are enough for exploring a variety of structures that may appear in the productive simulations. Our dataset not only includes the local minima, but also the trajectories lead to them, which helps MLPs learn those distorted structures away from minima. Though their structures are not distinguished from others, the transition pathways among local minima would be probably sampled, for example, in high-temperature MD simulations. If chemical reactions are heavily involved, reaction sampling methods should be used for an effective exploration.⁵⁴

With continuously growing interest in operando modeling,⁸⁸ such physically motivated simulations would greatly contribute to the investigation of dynamic changes of active sites in heterogeneous catalysis. GCMC ensures that the exploration is controlled by statistical mechanics, avoiding the exhausting search for low-energy configurations. Although GCMC still requires intensive calculations, this situation can be alleviated by using MLPs as we have done in this work. The structure evolution in the simulation offers valuable insights into the oxidation process, which can be further investigated by a more accurate method such as DFT with relatively small model systems. With the large-scale simulation powered by MLPs, the configuration possibilities have become large. Although the surface would inevitably become disordered in our simulations, we could still obtain the key characteristics of the oxidation mechanism and extract more distinct local chemical environments that are important for reactivity compared to standard DFT calculations. In this work, the important oxide intermediates can be observed from the GCMC trajectories with their formation processes elucidated, namely, the square

planar PtO₄ unit, the Pt₂O₆ stripe, the PtO₃ chain, and the octahedral PtO₆ unit.

Understanding the structures of the amorphous oxide surfaces can be essential to the investigation of heterogeneous catalysis.⁸⁵ The disordered oxide surfaces may provide distinct active sites that are critical for catalytic activity. Although some insights have been obtained from manually constructed surfaces,^{9–11} the accurate assessment of catalytic reactivities should be the average effect of all active sites explored within an accessible energy range.^{89–91} Such an ensemble of active sites can only be determined by heuristic structure search such as global optimization methods and GCMC adopted in this work, and the latter method generates more realistic structures since it offers a history-dependent trajectory.

With these advanced tools, computational catalysis can then reach another level of predictivity to elucidate catalyst structures. These methods require vast exploration of the configuration space, which can be largely accelerated by MLPs. In addition, many studies demonstrate that the coverage of surface adsorbates plays an important role in catalytic reactivity.^{77,92–95} Our simulations show that disordered structures appear on the surface at low coverage (~0.5 ML). These disordered structures should be taken into consideration when constructing surface models for microkinetic studies since they may contribute to a large portion of the reactivity. Furthermore, with the help of MLPs, we can develop off-lattice microkinetic algorithms with on-the-fly thermodynamic calculations to obtain better kinetic results.

5. CONCLUSIONS

In this work, we developed a training workflow to build MLPs applicable to complicated chemical systems. Two sampling algorithms, MD and GA, were used to explore distinct configurations for the dataset construction. The established PtO_x EANNP can well reproduce the physical properties of bulk Pt and its common oxides, such as the lattice constants, the surface energies, and the oxygen adsorption energies. Furthermore, we utilized the committee model strategy to estimate the uncertainty of model predictions, which helps us select unlearned structures and monitor the quality of productive simulations. With this well-validated potential, we performed GCMC simulations to observe the oxidation process of flat and stepped Pt surfaces based on large-scale models that contain thousands of atoms, which would be difficult to simulate using standard DFT calculations. According to the structure evolution in the simulations, we discovered the formation mechanism of two important surface oxides on the flat and stepped Pt surfaces, namely, the square planar PtO₄, the minimal Pt₂O₆ stripe, and one oxidized edge motif, the octahedral PtO₆ unit. The PtO₄ unit is the origin of the surface buckling, while the Pt₂O₆ stripe is the fundamental of the PtO₂ stripe growth. The octahedral PtO₆ unit formed on the edge involves the formation of sub-edge O atoms, which follows two migration mechanisms via a PtO₃ edge-chain. Our work demonstrated that the large-scale simulation using MLP could be a new workflow to investigate large complicated chemical systems and to provide ample insights into heterogeneous catalysis.

■ ASSOCIATED CONTENT

SI Supporting Information

The Supporting Information is available free of charge at <https://pubs.acs.org/doi/10.1021/acscatal.2c03976>.

Embedded atom neural network architecture, GCMC algorithm, training pipeline, full list of dataset, lattice constants and surface energies, oxygen diffusion pathway on the flat Pt(111) surface, uncertainty estimation by the committee model, and adsorption sites on the flat and stepped Pt surfaces (PDF)

AUTHOR INFORMATION

Corresponding Author

P. Hu – School of Chemistry and Chemical Engineering, Queen's University Belfast, Belfast BT9 SAG, U.K.; orcid.org/0000-0002-6318-1051; Email: p.hu@qub.ac.uk

Authors

Jiayan Xu – School of Chemistry and Chemical Engineering, Queen's University Belfast, Belfast BT9 SAG, U.K.; orcid.org/0000-0001-9897-5778

Wenbo Xie – School of Chemistry and Chemical Engineering, Queen's University Belfast, Belfast BT9 SAG, U.K.; orcid.org/0000-0001-5321-2494

Yulan Han – School of Chemistry and Chemical Engineering, Queen's University Belfast, Belfast BT9 SAG, U.K.

Complete contact information is available at:

<https://pubs.acs.org/10.1021/acscatal.2c03976>

Notes

The authors declare no competing financial interest.

ACKNOWLEDGMENTS

The NSFC (92045303) and NKRDP (2021YFA1500700) are acknowledged. We are grateful for access to the Queen's University Belfast Kelvin HPC service, which is partially funded by ESPRC (EP/T022175/1). We are grateful for computational support from the ARCHER2 UK National Supercomputing Service (<https://www.archer2.ac.uk>) for which access was obtained via the UKCP. J.X. acknowledges the financial support from the Queen's University Belfast and China Scholarship Council. Structures from GCMC trajectories displayed in this article are visualized using OVITO.⁹⁶

REFERENCES

- (1) Weaver, J. F. Surface Chemistry of Late Transition Metal Oxides. *Chem. Rev.* **2013**, *113*, 4164–4215.
- (2) van Spronsen, M. A.; Frenken, J. W. M.; Groot, I. M. N. Surface Science under Reaction Conditions: CO Oxidation on Pt and Pd Model Catalysts. *Chem. Soc. Rev.* **2017**, *46*, 4347–4374.
- (3) Hendriksen, B. L.; Frenken, J. W. CO Oxidation on Pt(110): Scanning Tunneling Microscopy inside a High-Pressure Flow Reactor. *Phys. Rev. Lett.* **2002**, *89*, No. 046101.
- (4) Li, W. X.; Osterlund, L.; Vestergaard, E. K.; Vang, R. T.; Matthiesen, J.; Pedersen, T. M.; Laegsgaard, E.; Hammer, B.; Besenbacher, F. Oxidation of Pt(110). *Phys. Rev. Lett.* **2004**, *93*, No. 146104.
- (5) Gong, X.-Q.; Raval, R.; Hu, P. General Insight into CO Oxidation: A Density Functional Theory Study of the Reaction Mechanism on Platinum Oxides. *Phys. Rev. Lett.* **2004**, *93*, No. 106104.
- (6) Pedersen, T. M.; Xue Li, W.; Hammer, B. Structure and Activity of Oxidized Pt(110) and A-PtO₂. *Phys. Chem. Chem. Phys.* **2006**, *8*, 1566–1574.
- (7) Zhu, Z.; Tao, F. F.; Zheng, F.; Chang, R.; Li, Y.; Heinke, L.; Liu, Z.; Salmeron, M.; Somorjai, G. A. Formation of Nanometer-Sized Surface Platinum Oxide Clusters on a Stepped Pt(557) Single Crystal Surface Induced by Oxygen: A High-Pressure STM and Ambient-Pressure XPS Study. *Nano Lett.* **2012**, *12*, 1491–1497.
- (8) Miller, D.; Sanchez Casalongue, H.; Bluhm, H.; Ogasawara, H.; Nilsson, A.; Kaya, S. Different Reactivity of the Various Platinum Oxides and Chemisorbed Oxygen in CO Oxidation on Pt(111). *J. Am. Chem. Soc.* **2014**, *136*, 6340–6347.
- (9) Ackermann, M. D.; Pedersen, T. M.; Hendriksen, B. L.; Robach, O.; Bobaru, S. C.; Popa, I.; Quiros, C.; Kim, H.; Hammer, B.; Ferrer, S.; et al. Structure and Reactivity of Surface Oxides on Pt(110) During Catalytic CO Oxidation. *Phys. Rev. Lett.* **2005**, *95*, No. 255505.
- (10) Wang, J. G.; Li, W. X.; Borg, M.; Gustafson, J.; Mikkelsen, A.; Pedersen, T. M.; Lundgren, E.; Weissenrieder, J.; Klikovits, J.; Schmid, M.; et al. One-Dimensional PtO₂ at Pt Steps: Formation and Reaction with CO. *Phys. Rev. Lett.* **2005**, *95*, No. 256102.
- (11) Li, W. X. Oxidation of Platinum Surfaces and Reaction with Carbon Monoxide. *J. Phys.: Condens. Matter* **2008**, *20*, No. 184022.
- (12) Butcher, D. R.; Grass, M. E.; Zeng, Z.; Aksoy, F.; Bluhm, H.; Li, W. X.; Mun, B. S.; Somorjai, G. A.; Liu, Z. In Situ Oxidation Study of Pt(110) and Its Interaction with CO. *J. Am. Chem. Soc.* **2011**, *133*, 20319–20325.
- (13) Weaver, J. F.; Chen, J.-J.; Gerrard, A. L. Oxidation of Pt(111) by Gas-Phase Oxygen Atoms. *Surf. Sci. Sci.* **2005**, *592*, 83–103.
- (14) Seriani, N.; Mittendorfer, F. Platinum-Group and Noble Metals under Oxidizing Conditions. *J. Phys.: Condens. Matter* **2008**, *20*, No. 184023.
- (15) Hawkins, J. M.; Weaver, J. F.; Asthagiri, A. Density Functional Theory Study of the Initial Oxidation of the Pt(111) Surface. *Phys. Rev. B* **2009**, *79*, No. 125434.
- (16) Bandlow, J.; Kaghazchi, P.; Jacob, T.; Papp, C.; Tränkenschuh, B.; Streber, R.; Lorenz, M. P. A.; Fuhrmann, T.; Denecke, R.; Steinrück, H. P. Oxidation of Stepped Pt(111) Studied by X-Ray Photoelectron Spectroscopy and Density Functional Theory. *Phys. Rev. B* **2011**, *83*, No. 174107.
- (17) Holby, E. F.; Greeley, J.; Morgan, D. Thermodynamics and Hysteresis of Oxide Formation and Removal on Platinum (111) Surfaces. *J. Phys. Chem. C* **2012**, *116*, 9942–9946.
- (18) Hanselman, S.; McCrum, I. T.; Rost, M. J.; Koper, M. T. M. Thermodynamics of the Formation of Surface PtO₂ Stripes on Pt(111) in the Absence of Subsurface Oxygen. *Phys. Chem. Chem. Phys.* **2020**, *22*, 10634–10640.
- (19) Reuter, K.; Scheffler, M. Composition, Structure, and Stability of RuO₂(110) as a Function of Oxygen Pressure. *Phys. Rev. B* **2001**, *65*, No. 035406.
- (20) Rogal, J.; Reuter, K.; Scheffler, M. CO Oxidation at Pd(100): A First-Principles Constrained Thermodynamics Study. *Phys. Rev. B* **2007**, *75*, No. 205433.
- (21) Getman, R. B.; Xu, Y.; Schneider, W. F. Thermodynamics of Environment-Dependent Oxygen Chemisorption on Pt(111). *J. Phys. Chem. C* **2008**, *112*, 9559–9572.
- (22) van Spronsen, M. A.; Frenken, J. W. M.; Groot, I. M. N. Observing the Oxidation of Platinum. *Nat. Commun.* **2017**, *8*, 429.
- (23) Schmidt, D. J.; Chen, W.; Wolverton, C.; Schneider, W. F. Performance of Cluster Expansions of Coverage-Dependent Adsorption of Atomic Oxygen on Pt(111). *J. Chem. Theory Comput.* **2012**, *8*, 264–273.
- (24) Wu, C.; Schmidt, D. J.; Wolverton, C.; Schneider, W. F. Accurate Coverage-Dependence Incorporated into First-Principles Kinetic Models: Catalytic NO Oxidation on Pt(111). *J. Catal.* **2012**, *286*, 88–94.
- (25) Cao, X.-M.; Shao, Z.-J.; Hu, P. A Fast Species Redistribution Approach to Accelerate the Kinetic Monte Carlo Simulation for Heterogeneous Catalysis. *Phys. Chem. Chem. Phys.* **2020**, *22*, 7348–7364.
- (26) Tang, H.; Van der Ven, A.; Trout, B. L. Phase Diagram of Oxygen Adsorbed on Platinum (111) by First-Principles Investigation. *Phys. Rev. B* **2004**, *70*, No. 045420.
- (27) Lachet, V.; Boutin, A.; Tavitian, B.; Fuchs, A. H. Grand Canonical Monte Carlo Simulations of Adsorption of Mixtures of

- Xylene Molecules in Faujasite Zeolites. *Faraday Discuss.* **1997**, *106*, 307–323.
- (28) Frenkel, D.; Smit, B. *Understanding Molecular Simulation: From Algorithms to Applications*, 2nd ed.; Academic Press, 2002; pp 126–135.
- (29) Wexler, R. B.; Qiu, T.; Rappe, A. M. Automatic Prediction of Surface Phase Diagrams Using Ab Initio Grand Canonical Monte Carlo. *J. Phys. Chem. C* **2019**, *123*, 2321–2328.
- (30) Valentini, P.; Schwartzentruber, T. E.; Cozmuta, I. ReaxFF Grand Canonical Monte Carlo Simulation of Adsorption and Dissociation of Oxygen on Platinum (111). *Surf. Sci.* **2011**, *605*, 1941–1950.
- (31) Fantauzzi, D.; Bandlow, J.; Sabo, L.; Mueller, J. E.; van Duin, A. C.; Jacob, T. Development of a ReaxFF Potential for Pt-O Systems Describing the Energetics and Dynamics of Pt-Oxide Formation. *Phys. Chem. Chem. Phys.* **2014**, *16*, 23118–23133.
- (32) Fantauzzi, D.; Mueller, J. E.; Sabo, L.; van Duin, A. C. T.; Jacob, T. Surface Buckling and Subsurface Oxygen: Atomistic Insights into the Surface Oxidation of Pt(111). *ChemPhysChem* **2015**, *16*, 2797–2802.
- (33) Gai, L.; Shin, Y. K.; Raju, M.; van Duin, A. C. T.; Raman, S. Atomistic Adsorption of Oxygen and Hydrogen on Platinum Catalysts by Hybrid Grand Canonical Monte Carlo/Reactive Molecular Dynamics. *J. Phys. Chem. C* **2016**, *120*, 9780–9793.
- (34) Fantauzzi, D.; Krick Calderon, S.; Mueller, J. E.; Grabau, M.; Papp, C.; Steinruck, H. P.; Senftle, T. P.; van Duin, A. C.; Jacob, T. Growth of Stable Surface Oxides on Pt(111) at near-Ambient Pressures. *Angew. Chem., Int. Ed.* **2017**, *56*, 2594–2598.
- (35) Kirchhoff, B.; Braunwarth, L.; Jung, C.; Jonsson, H.; Fantauzzi, D.; Jacob, T. Simulations of the Oxidation and Degradation of Platinum Electrocatalysts. *Small* **2020**, *16*, No. e1905159.
- (36) Xu, J.; Cao, X. M.; Hu, P. Perspective on Computational Reaction Prediction Using Machine Learning Methods in Heterogeneous Catalysis. *Phys. Chem. Chem. Phys.* **2021**, *23*, 11155–11179.
- (37) Behler, J. Four Generations of High-Dimensional Neural Network Potentials. *Chem. Rev.* **2021**, *121*, 10037–10072.
- (38) Ko, T. W.; Finkler, J. A.; Goedecker, S.; Behler, J. A Fourth-Generation High-Dimensional Neural Network Potential with Accurate Electrostatics Including Non-Local Charge Transfer. *Nat. Commun.* **2021**, *12*, 398.
- (39) Zhang, Y.; Xia, J.; Jiang, B. Physically Motivated Recursively Embedded Atom Neural Networks: Incorporating Local Completeness and Nonlocality. *Phys. Rev. Lett.* **2021**, *127*, No. 156002.
- (40) Batzner, S.; Musaelian, A.; Sun, L.; Geiger, M.; Mailoa, J. P.; Kornbluth, M.; Molinari, N.; Smidt, T. E.; Kozinsky, B. E(3)-Equivariant Graph Neural Networks for Data-Efficient and Accurate Interatomic Potentials. *Nat. Commun.* **2022**, *13*, 2453.
- (41) Unke, O. T.; Chmiela, S.; Gastegger, M.; Schutt, K. T.; Sauceda, H. E.; Muller, K. R. Spookynet: Learning Force Fields with Electronic Degrees of Freedom and Nonlocal Effects. *Nat. Commun.* **2021**, *12*, 7273.
- (42) Open Catalyst Project. <https://opencatalystproject.org/> (accessed September 20, 2022), DOI: 10.3390/membranes12101001.
- (43) Peterson, A. A.; Christensen, R.; Khorshidi, A. Addressing Uncertainty in Atomistic Machine Learning. *Phys. Chem. Chem. Phys.* **2017**, *19*, 10978–10985.
- (44) Zhang, L.; Lin, D.-Y.; Wang, H.; Car, R.; Weinan, E. Active Learning of Uniformly Accurate Interatomic Potentials for Materials Simulation. *Phys. Rev. Mater.* **2019**, *3*, No. 023804.
- (45) Musil, F.; Willatt, M. J.; Langovoy, M. A.; Ceriotti, M. Fast and Accurate Uncertainty Estimation in Chemical Machine Learning. *J. Chem. Theory Comput.* **2019**, *15*, 906–915.
- (46) Tran, K.; Neiswanger, W.; Yoon, J.; Zhang, Q.; Xing, E.; Ulissi, Z. W. Methods for Comparing Uncertainty Quantifications for Material Property Predictions. *Mach. Learn.: Sci. Technol.* **2020**, *1*, No. 025006.
- (47) Novikov, I. S.; Shapeev, A. V. Improving Accuracy of Interatomic Potentials: More Physics or More Data? A Case Study of Silica. *Mater. Today Commun.* **2019**, *18*, 74–80.
- (48) Schran, C.; Brezina, K.; Marsalek, O. Committee Neural Network Potentials Control Generalization Errors and Enable Active Learning. *J. Chem. Phys.* **2020**, *153*, 104105.
- (49) Shuaibi, M.; Sivakumar, S.; Chen, R. Q.; Ulissi, Z. W. Enabling Robust Offline Active Learning for Machine Learning Potentials Using Simple Physics-Based Priors. *Mach. Learn.: Sci. Technol.* **2021**, *2*, No. 025007.
- (50) Imbalzano, G.; Zhuang, Y.; Kapil, V.; Rossi, K.; Engel, E. A.; Grasselli, F.; Ceriotti, M. Uncertainty Estimation for Molecular Dynamics and Sampling. *J. Chem. Phys.* **2021**, *154*, No. 074102.
- (51) Lin, Q.; Zhang, L.; Zhang, Y.; Jiang, B. Searching Configurations in Uncertainty Space: Active Learning of High-Dimensional Neural Network Reactive Potentials. *J. Chem. Theory Comput.* **2021**, *17*, 2691–2701.
- (52) Janet, J. P.; Duan, C.; Yang, T.; Nandy, A.; Kulik, H. J. A Quantitative Uncertainty Metric Controls Error in Neural Network-Driven Chemical Discovery. *Chem. Sci.* **2019**, *10*, 7913–7922.
- (53) Vandermause, J.; Torrisi, S. B.; Batzner, S.; Xie, Y.; Sun, L.; Kolpak, A. M.; Kozinsky, B. On-the-Fly Active Learning of Interpretable Bayesian Force Fields for Atomistic Rare Events. *npj Comput. Mater.* **2020**, *6*, 20.
- (54) Xu, J.; Cao, X. M.; Hu, P. Accelerating Metadynamics-Based Free-Energy Calculations with Adaptive Machine Learning Potentials. *J. Chem. Theory Comput.* **2021**, *17*, 4465–4476.
- (55) Wen, M.; Tadmor, E. B. Uncertainty Quantification in Molecular Simulations with Dropout Neural Network Potentials. *npj Comput. Mater.* **2020**, *6*, 124.
- (56) Kresse, G.; Furthmüller, J. Efficiency of Ab-Initio Total Energy Calculations for Metals and Semiconductors Using a Plane-Wave Basis Set. *Comput. Mater. Sci.* **1996**, *6*, 5–50.
- (57) Kresse, G.; Furthmüller, J. Efficient Iterative Schemes for Ab Initio Total-Energy Calculations Using a Plane-Wave Basis Set. *Phys. Rev. B* **1996**, *54*, 11169.
- (58) Dion, M.; Rydberg, H.; Schroder, E.; Langreth, D. C.; Lundqvist, B. I. Van der Waals Density Functional for General Geometries. *Phys. Rev. Lett.* **2004**, *92*, No. 246401.
- (59) Roman-Perez, G.; Soler, J. M. Efficient Implementation of a van der Waals Density Functional: Application to Double-Wall Carbon Nanotubes. *Phys. Rev. Lett.* **2009**, *103*, No. 096102.
- (60) Klimeš, J.; Bowler, D. R.; Michaelides, A. Van der Waals Density Functionals Applied to Solids. *Phys. Rev. B* **2011**, *83*, No. 195131.
- (61) Monkhorst, H. J.; Pack, J. D. Special Points for Brillouin-Zone Integrations. *Phys. Rev. B* **1976**, *13*, 5188–5192.
- (62) Zhang, Y.; Hu, C.; Jiang, B. Embedded Atom Neural Network Potentials: Efficient and Accurate Machine Learning with a Physically Inspired Representation. *J. Phys. Chem. Lett.* **2019**, *10*, 4962–4967.
- (63) Zhang, Y.; Xia, J.; Jiang, B. Reann: A Pytorch-Based End-to-End Multi-Functional Deep Neural Network Package for Molecular, Reactive, and Periodic Systems. *J. Chem. Phys.* **2022**, *156*, 114801.
- (64) Zhang, Y.; Hu, C.; Jiang, B. Accelerating Atomistic Simulations with Piecewise Machine-Learned Ab Initio Potentials at a Classical Force Field-Like Cost. *Phys. Chem. Chem. Phys.* **2021**, *23*, 1815–1821.
- (65) Senftle, T. P.; Meyer, R. J.; Janik, M. J.; van Duin, A. C. Development of a ReaxFF Potential for Pdo and Application to Palladium Oxide Formation. *J. Chem. Phys.* **2013**, *139*, No. 044109.
- (66) Senftle, T. P.; van Duin, A. C. T.; Janik, M. J. Determining In Situ Phases of a Nanoparticle Catalyst Via Grand Canonical Monte Carlo Simulations with the ReaxFF Potential. *Catal. Commun.* **2014**, *S2*, 72–77.
- (67) Thompson, A. P.; Aktulga, H. M.; Berger, R.; Bolintineanu, D. S.; Brown, W. M.; Crozier, P. S.; Int Veld, P. J.; Kohlmeyer, A.; Moore, S. G.; Nguyen, T. D.; et al. Lammps - a Flexible Simulation Tool for Particle-Based Materials Modeling at the Atomic, Meso, and Continuum Scales. *Comput. Phys. Commun.* **2022**, *271*, No. 108171.
- (68) Hjorth Larsen, A.; Jorgen Mortensen, J.; Blomqvist, J.; Castelli, I. E.; Christensen, R.; Dulak, M.; Friis, J.; Groves, M. N.; Hammer, B.; Hargus, C.; et al. The Atomic Simulation Environment-a Python

- Library for Working with Atoms. *J. Phys.: Condens. Matter* **2017**, *29*, 273002.
- (69) Vilhelmsen, L. B.; Hammer, B. A Genetic Algorithm for First Principles Global Structure Optimization of Supported Nano Structures. *J. Chem. Phys.* **2014**, *141*, No. 044711.
- (70) Mahoney, M. W.; Drineas, P. CUR Matrix Decompositions for Improved Data Analysis. *Proc. Natl. Acad. Sci. U. S. A.* **2009**, *106*, 697–702.
- (71) Bernstein, N.; Csányi, G.; Deringer, V. L. De Novo Exploration and Self-Guided Learning of Potential-Energy Surfaces. *npj Comput. Mater.* **2019**, *5*, 99.
- (72) Xu, J. Generating Deep Potential with Python (GDPy). <https://github.com/hsulab/GDPy> (accessed September 20, 2022).
- (73) Nomiyama, R. K.; Piotrowski, M. J.; Da Silva, J. L. F. Bulk Structures of PtO and PtO₂ from Density Functional Calculations. *Phys. Rev. B* **2011**, *84*, No. 100101.
- (74) Seriani, N.; Pompe, W.; Ciacchi, L. C. Catalytic Oxidation Activity of Pt₃O₄ Surfaces and Thin Films. *J. Phys. Chem. B* **2006**, *110*, 14860–14869.
- (75) Yang, Y.; Kawazoe, Y. Adsorption and Diffusion of H Atoms on β-PtO₂ Surface: The Role of Nuclear Quantum Effects. *J. Phys. Chem. C* **2019**, *123*, 13804–13811.
- (76) Deshpande, S.; Maxson, T.; Greeley, J. Graph Theory Approach to Determine Configurations of Multidentate and High Coverage Adsorbates for Heterogeneous Catalysis. *npj Comput. Mater.* **2020**, *6*, 79.
- (77) Ding, Y.; Xu, Y.; Song, Y.; Guo, C.; Hu, P. Quantitative Studies of the Coverage Effects on Microkinetic Simulations for No Oxidation on Pt(111). *J. Phys. Chem. C* **2019**, *123*, 27594–27602.
- (78) Lym, J.; Gu, G. H.; Jung, Y.; Vlachos, D. G. Lattice Convolutional Neural Network Modeling of Adsorbate Coverage Effects. *J. Phys. Chem. C* **2019**, *123*, 18951–18959.
- (79) Devarajan, S. P.; Hinojosa, J. A.; Weaver, J. F. STM Study of High-Coverage Structures of Atomic Oxygen on Pt(111): P(2×1) and Pt Oxide Chain Structures. *Surf. Sci.* **2008**, *602*, 3116–3124.
- (80) Miller, D. J.; Oberg, H.; Kaya, S.; Sanchez Casalongue, H.; Friebel, D.; Anniyev, T.; Ogasawara, H.; Bluhm, H.; Pettersson, L. G.; Nilsson, A. Oxidation of Pt(111) under near-Ambient Conditions. *Phys. Rev. Lett.* **2011**, *107*, No. 195502.
- (81) Feibelman, P. J.; Esch, S.; Michely, T. O Binding Sites on Stepped Pt(111) Surfaces. *Phys. Rev. Lett.* **1996**, *77*, 2257–2260.
- (82) Ogawa, T.; Kuwabara, A.; Fisher, C. A. J.; Moriwake, H.; Miwa, T. Adsorption and Diffusion of Oxygen Atoms on a Pt(211) Stepped Surface. *J. Phys. Chem. C* **2013**, *117*, 9772–9778.
- (83) Ogawa, T.; Kuwabara, A.; Fisher, C. A. J.; Moriwake, H. A Density Functional Study of Oxygen Adatoms on a Step-Doubled Platinum Surface. *J. Phys. Chem. C* **2014**, *118*, 23675–23681.
- (84) Cheng, X.; Wang, Z.; Mao, Y.; Hu, P. Evidence of the O-Pd-O and Pd-O₄ Structure Units as Oxide Seeds and Their Origin on Pd(211): Revealing the Mechanism of Surface Oxide Formation. *Phys. Chem. Chem. Phys.* **2019**, *21*, 6499–6505.
- (85) Bunting, R. J.; Cheng, X.; Thompson, J.; Hu, P. Amorphous Surface Pdo_x and Its Activity toward Methane Combustion. *ACS Catal.* **2019**, *9*, 10317–10323.
- (86) Wang, Z.; Hu, P. Identifying the General Trend of Activity of Non-Stoichiometric Metal Oxide Phases for CO Oxidation on Pd(111). *Sci. China Chem.* **2019**, *62*, 784–789.
- (87) Henkelman, G.; Uberuaga, B. P.; Jónsson, H. A Climbing Image Nudged Elastic Band Method for Finding Saddle Points and Minimum Energy Paths. *J. Chem. Phys.* **2000**, *113*, 9901–9904.
- (88) Shi, X.; Lin, X.; Luo, R.; Wu, S.; Li, L.; Zhao, Z.-J.; Gong, J. Dynamics of Heterogeneous Catalytic Processes at Operando Conditions. *JACS Au* **2021**, *1*, 2100–2120.
- (89) Sun, G.; Sautet, P. Metastable Structures in Cluster Catalysis from First-Principles: Structural Ensemble in Reaction Conditions and Metastability Triggered Reactivity. *J. Am. Chem. Soc.* **2018**, *140*, 2812–2820.
- (90) Zhang, Z.; Zandkarimi, B.; Alexandrova, A. N. Ensembles of Metastable States Govern Heterogeneous Catalysis on Dynamic Interfaces. *Acc. Chem. Res.* **2020**, *53*, 447–458.
- (91) Lee, M.-H.; Xu, J.; Xie, W. Exploring the Stability of Single-Atom Catalysts Using the Density Functional Theory-Based Global Optimization Method: H₂ Formation on VO_x/γ-Al₂O₃(100). *J. Phys. Chem. C* **2022**, *126*, 6973–6981.
- (92) Guo, C.; Mao, Y.; Yao, Z.; Chen, J.; Hu, P. Examination of the Key Issues in Microkinetics: CO Oxidation on Rh(1 1 1). *J. Catal.* **2019**, *379*, 52–59.
- (93) Xie, W.; Xu, J.; Ding, Y.; Hu, P. Quantitative Studies of the Key Aspects in Selective Acetylene Hydrogenation on Pd(111) by Microkinetic Modeling with Coverage Effects and Molecular Dynamics. *ACS Catal.* **2021**, *11*, 4094–4106.
- (94) Xie, W.; Hu, P. Influence of Surface Defects on Activity and Selectivity: A Quantitative Study of Structure Sensitivity of Pd Catalysts for Acetylene Hydrogenation. *Catal. Sci. Technol.* **2021**, *11*, 5212–5222.
- (95) Xie, W.; Xu, J.; Chen, J.; Wang, H.; Hu, P. Achieving Theory-Experiment Parity for Activity and Selectivity in Heterogeneous Catalysis Using Microkinetic Modeling. *Acc. Chem. Res.* **2022**, *55*, 1237–1248.
- (96) Stukowski, A. Visualization and Analysis of Atomistic Simulation Data with Ovito—the Open Visualization Tool. *Modell. Simul. Mater. Sci. Eng.* **2010**, *18*, No. 015012.

□ Recommended by ACS

Enhancing the Performance of Global Optimization of Platinum Cluster Structures by Transfer Learning in a Deep Neural Network

Qi Yang, Sheng-Gui He, et al.

MARCH 14, 2023

JOURNAL OF CHEMICAL THEORY AND COMPUTATION

READ ▶

Catalytic Activity Maps for Alloy Nanoparticles

Liang Cao and Tim Mueller

MARCH 27, 2023

JOURNAL OF THE AMERICAN CHEMICAL SOCIETY

READ ▶

Atomic-Scale Mechanism of Platinum Catalyst Restructuring under a Pressure of Reactant Gas

Vaidish Sumaria, Philippe Sautet, et al.

DECEMBER 22, 2022

JOURNAL OF THE AMERICAN CHEMICAL SOCIETY

READ ▶

Exploring the Composition Space of High-Entropy Alloy Nanoparticles for the Electrocatalytic H₂/CO Oxidation with Bayesian Optimization

Vladislav A. Mints, Matthias Arenz, et al.

SEPTEMBER 01, 2022

ACS CATALYSIS

READ ▶

Get More Suggestions >